Supporting Information

An Antiferromagnetic Metalloring Pyrazolate (Pz) Framework with $[Cu_{12}(\mu_2\text{-}OH)_{12}(Pz)_{12}]$ Nodes for Separation of C_2H_2/CH_4 Mixture

Ziyin Li,[a] Yingxiang Ye,[a] Zizhu Yao,[a] Junzhi Guo,[a] Quanjie Lin,[a] Jindan, Zhang,[a] Zhangjing Zhang,[*ab] Fangfang Wei[*a] and Shengchang Xiang[*ab]

[a]*Fujian Provincial Key Laboratory of Polymer Materials, College of Chemistry and Materials Science, Fujian Normal University, 32 Shangsan Road, Fuzhou 350007, PR China*

[b]*State Key Laboratory of Structural Chemistry, Fujian Institute of Research on the Structure of Matter, Chinese Academy of Sciences, Fuzhou, Fujian 350002, PR China*

E-mail: zzhang@fjnu.edu.cn; wfanfan@fjnu.edu.cn; scxiang@fjnu.edu.cn.

Content

Gas Sorption Measurements. After the bulk of the solvent was decanted, the freshly prepared sample of **MROF-12** (~0.15 g) was soaked in ~10 mL acetone for 1 h, and then the solvent was decanted. Following the procedure of acetone soaking and decanting for ten times, the solvent-exchange samples were activated by vacuum at 60 ^{o}C for 24 hours till the pressure of 5 μmHg. N_2, CO_2, methane, ethylene, ethane and acetylene adsorption isotherms were measured on Micromeritics ASAP 2020 HD88 surface are analyzer for the **MROF-12a**. The sorption measurement was maintained at 77 K with liquid nitrogen and at 273 K with an ice-water bath (slush), respectively.

Virial Equation Analysis. The virial equation can be written[1] as follows:

$$\ln(n/p) = A_0 + A_1 n + A_2 n^2 + \cdots \qquad (1)$$

where n is the amount adsorbed (mol g^{-1}) at pressure p (Pa). At a low surface coverage, the A_2 and higher terms can be neglected and the equation becomes

$$\ln(n/p) = A_0 + A_1 n \qquad (2)$$

A linear graph of ln(n/p) versus n was obtained at low surface coverage and this is consistent with neglecting the higher terms in eqn (2). A_0 is related to the adsorbate-adsorbent interactions, Whereas A_1 describes the adsorbate-adsorbate interactions. The virial parameters are given in **Table S4**, Supporting Information.

Enthalpies of Adsorption. Zero surface coverage. The isosteric enthalpies of adsorption at zero surface coverage (Q_{st}, $n=0$) are a fundamental measure of adsorbate-adsorbent interactions and these values were calculated from the A_0 values obtained by extrapolation of the virial graph to zero surface coverage.

van't Hoff isochore. The isosteric enthalpies of adsorption as a function of surface coverage were calculated from the isotherms using the van't Hoff isochore, which is given by the equation

$$\ln(p) = -\frac{\Delta H}{RT} + \frac{\Delta S}{R} \qquad (3)$$

A graph of ln P *versus* 1/T at a constant amount adsorbed (n) allows the isosteric enthalpy and entropy of adsorption to be determined. The pressure values for a specific amount adsorbed were calculated from the adsorption isotherms by: (1) assuming a linear relationship between the adjacent isotherm points starting from the first isotherm point; and (2) using the virial equation at low surface coverage. The agreements between the two methods for **MROF-12a** are shown in Figure S14.

Prediction of the Gas Adsorption Selectivity by IAST. The ideal adsorption solution theory (IAST)[2] was used to predict the binary mixture adsorption from the experimental pure gas isotherms. To perform the integrations required by IAST, single-component isotherms should be fitted by the correct model. In practice, several methods are available; for this set of data we found that the single-site Langmuir-Freundlich equation was successful in fitting the results.

$$N = N^{\max} \times \frac{bp^{1/n}}{1 + bp^{1/n}} \qquad (4)$$

where P is the pressure of the bulk gas in equilibrium with the adsorbed phase (kPa), N is the amount adsorbed per mass of adsorbent (mmol g^{-1}), N^{max} is the saturation capacities of site 1 (mmol g^{-1}), b is the affinity coefficients of site 1 (1/kPa) and n represents the deviations from an ideal homogeneous surface. The fitted parameters were then used to predict multi-component adsorption with IAST. The adsorption selectivities based on IAST for mixed C_2H_2/CH_4, C_2H_4/CH_4, and C_2H_6/CH_4 are defined by the following equation:

$$S_{A/B} = (x_A/y_A)/(x_B/y_B) \qquad (5)$$

where x_i and y_i are the mole fractions of component i (i = A, B) in the adsorbed and bulk phases, respectively.

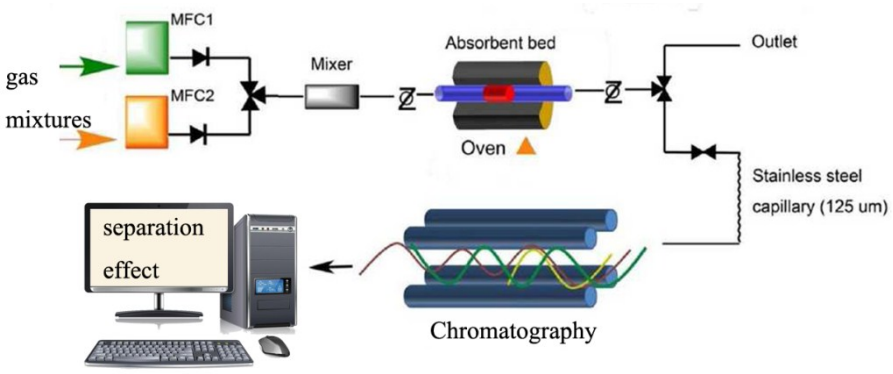

Scheme S1. Illustration of a lab-scale fix-bed reactor.

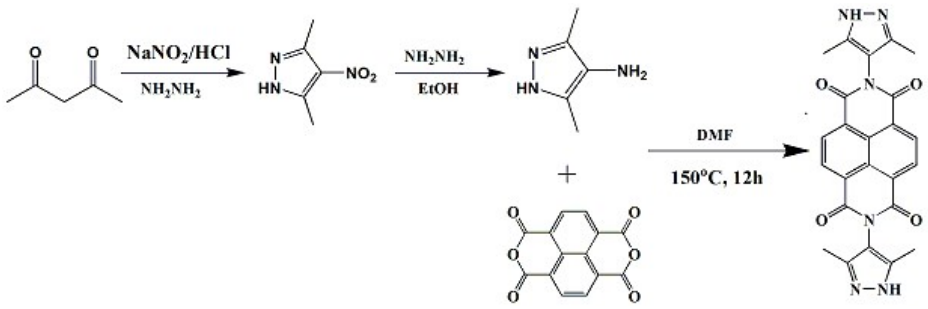

Scheme S2. Synthesis of 4-amine-3,5-dimethyl-1H-pyrazole and H_2NDI.

Synthesis of 4-amine-3,5-dimethyl-1H-pyrazole.

This was prepared as described previously.[3] The acetylacetone (20 g, 0.2 mol) was added to the solution of concentrated HCl (18 mL, 0.6 mol) and deionized water (100 mL, 5.55 mol), then stir in the ice water bath (8 ^{o}C). Sodium nitrite solution (14 g, 0.2 mol) was drop into the above solution, standing for 20 min. Opening electric stirring, 85% hydrazine hydrate (12 g, 0.2 mol) was added to reaction which will form a large number of blue recipitate. Continue adding ethanol (100 mL, 2.6 mol) till the blue precipitate were dissolved completely, then adjusted the pH to neutral. Hydrazine hydrate (13.5 g, 0.22 mol) was added dropwise to the above solution, maintaining the temperature at 80 ^{o}C for 5 h until the solution of reaction turned golden yellow. Finally, the solvent was evaporated and the desired product was washed with cold ethanol for three times, then collected by filtration and dried in 60 ^{o}C to afford white powders. (Yield 50.6% based on acetylacetone).

Synthesis of H_2NDI.

H_2NDI were prepared as described previously with some modification.[1] A dry 100 mL Schlenk flask was charged with 1,4,5,8-naphthalenetetra carboxylic dianhydride (0.86 g, 3.2 mmol), 3,5-dimethylpyrazole (0.75 g, 6.8 mmol), and anhydrous DMF (50 mL) under a nitrogen atmosphere. The reaction mixture was heated at 150 ^{o}C with rapid stirring for 12 hours. The flask was cooled to room temperature and the dark brown DMF solution was poured into stirring diethyl ether (150 mL). The precipitated yellow solid was separated by filtration and recrystallized from DMF/diethyl ether/H_2O (10 mL: 15 mL: 5mL). The product was filtered and dried *in vacuo* at 70 ^{o}C to afford 1.2 g (Yield 82% based on 1,4,5,8-naphthalenetetracarboxylicdianhydride) of light yellow crystals.

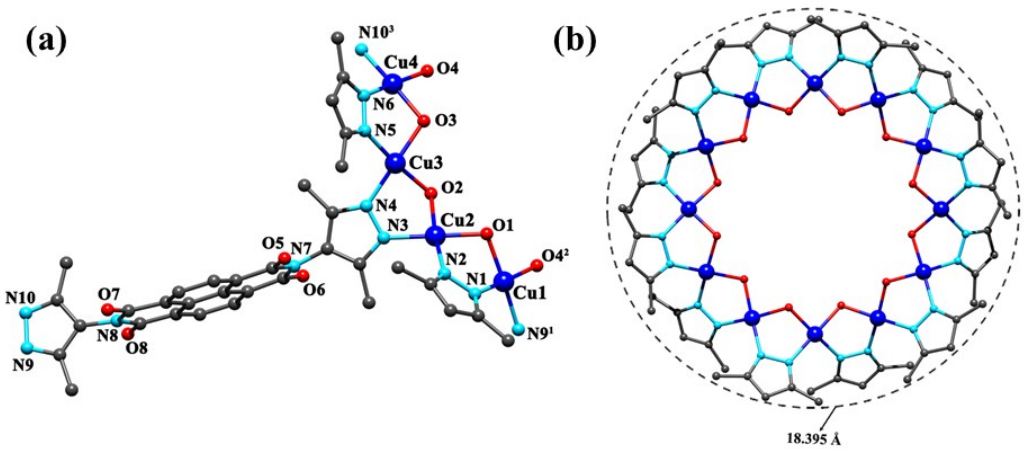

Figure S1. (a) The coordination environments of the Cu^{2+} atoms (Symmetry codes: [1] = -1+*y*-*x*, -1-*x*, 1+*z*; [2] = -y, +*x*-*y*, +*z*; [3] = -y, 1+*x*-*y*, 1+*z*). (b) The $[Cu_{12}(\mu_2\text{-}OH)_{12}(Pz)_{12}]$ metalloring SBU with a outer diameter of 18.412 Å.

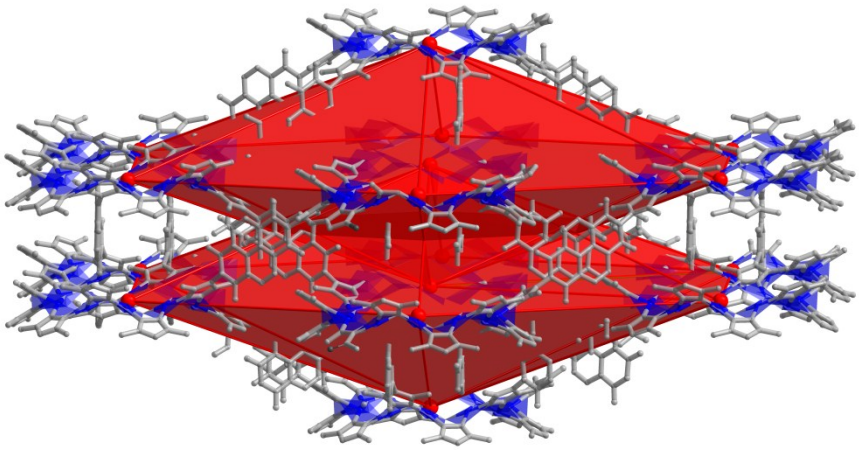

Figure S2. Self-interlock of Cages I viewed from the *c*-axis.

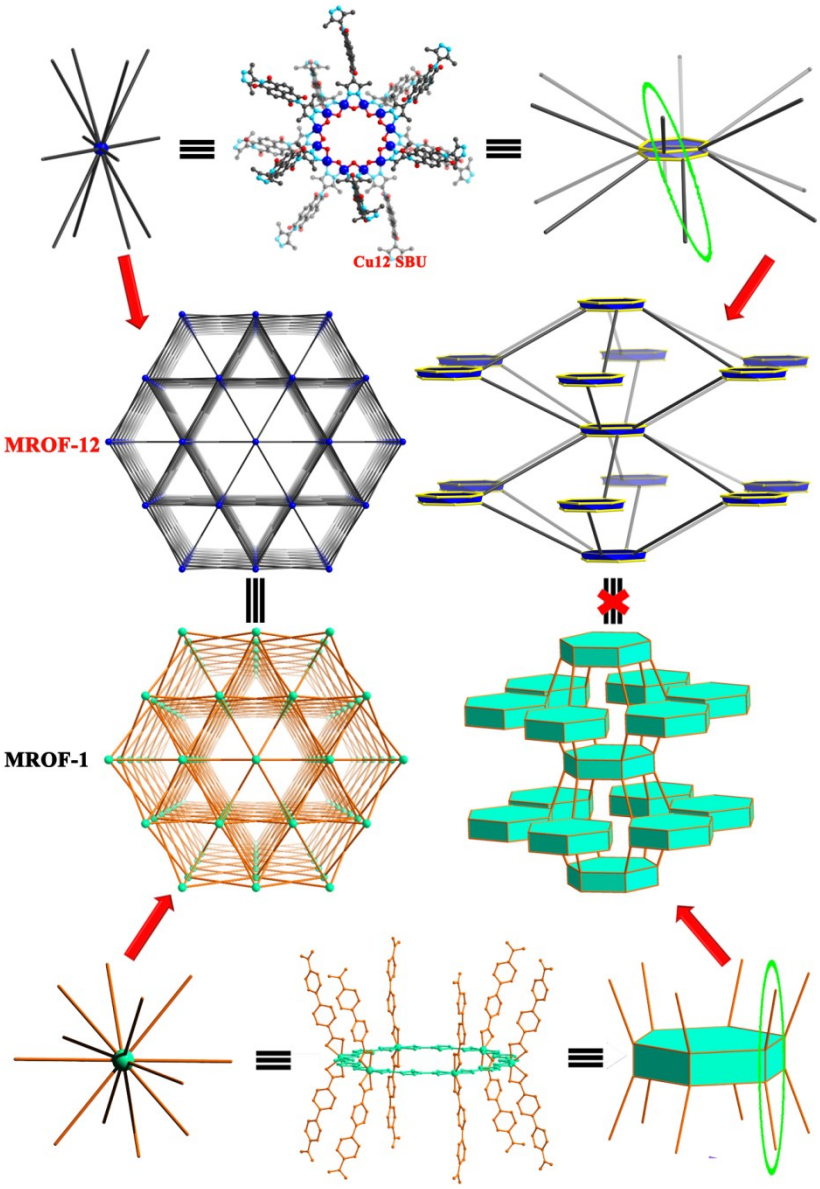

Figure S3. The comparison of the topological analysis for **MROF-12** and MROF-1[4]. The stacking mode of 3D structure for them are different, considering the 12-connected clusters in them as hexagonal antiprism ($[Cu_{12}(\mu_2\text{-}OH)_{12}(Pz)_{12}]$ SBU) and hexagonal prism ($[In_6(thb)_6]^{6+}$ metalloring SBU) respectively, which mainly due to the torsional difference between the 12-connected polyhedral prisms (green ellipse) in the two cluster nodes.

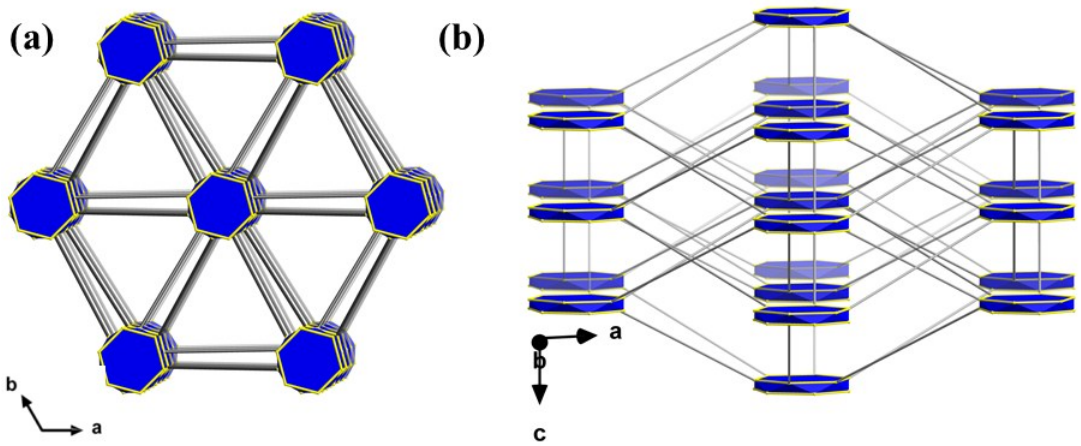

Figure S4. Schematic representation of the 12-connected topology along *c* and *b* axis for **MROF-12**.

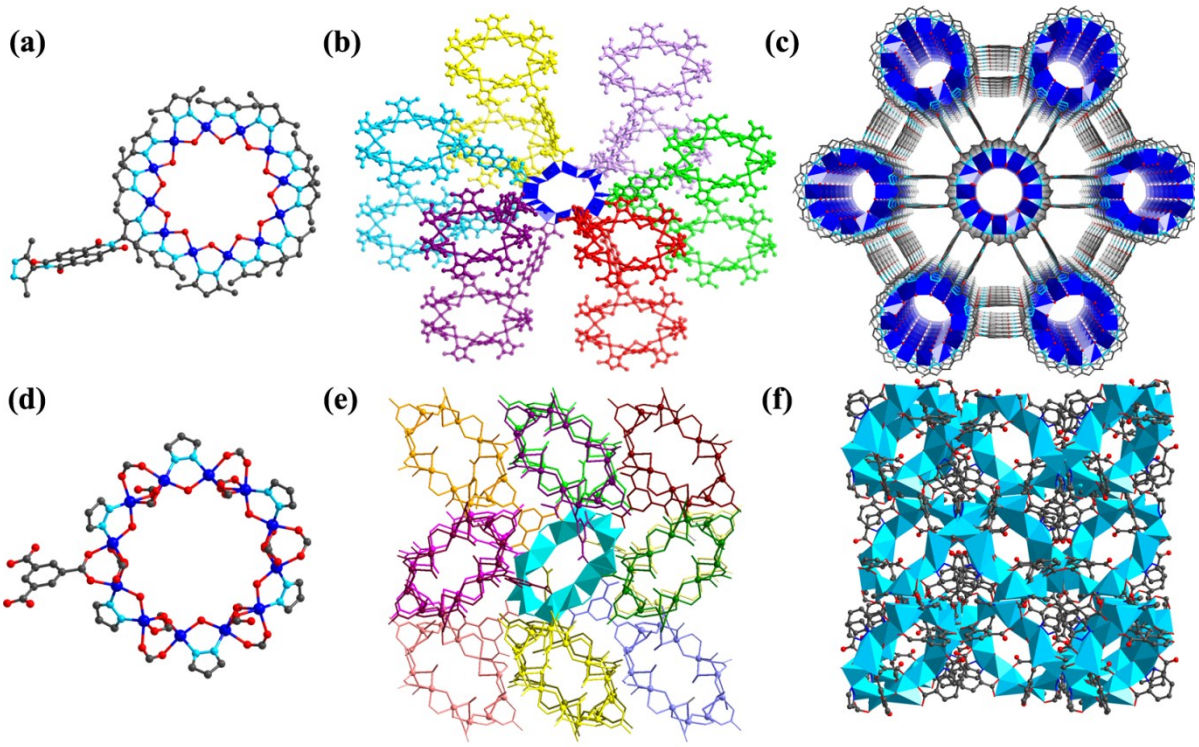

Figure S5. The comparison of the $[Cu_{12}(\mu_2\text{-}OH)_{12}(Pz)_{12}]$ metalloring clusters (a), the connection of metalloring clusters (b) and 3D frameworks (c) for **MROF-12** and $H_2Na_4[Cu_{12}(OH)_6(pz)_6(BTC)_6]\cdot 23H_2O$[5].

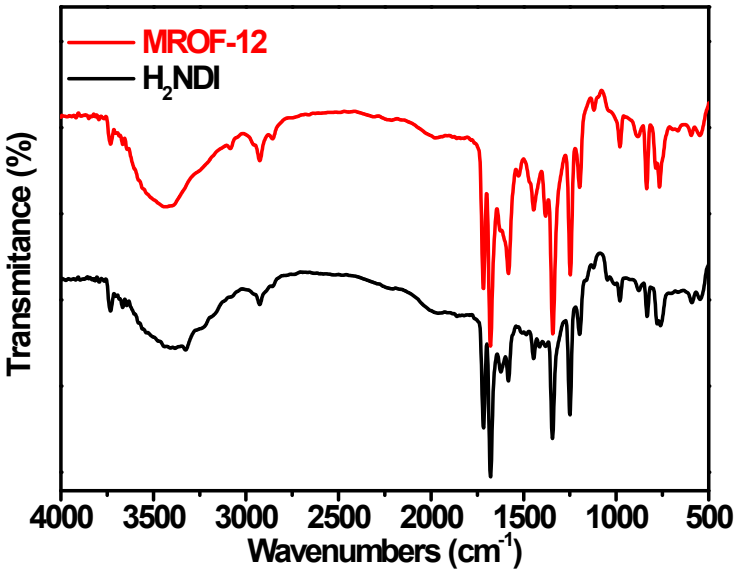

Figure S6. IR spectrum of **MROF-12** and H_2NDI.

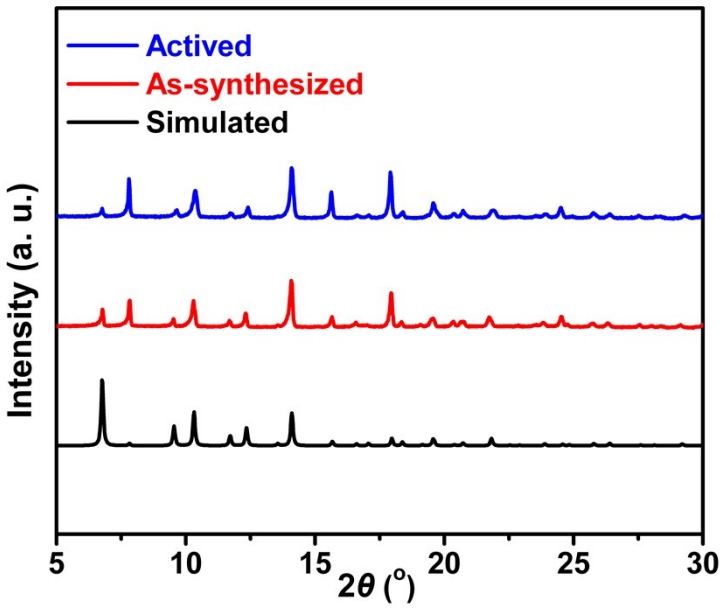

Figure S7. Powder X-ray diffraction (PXRD) patterns for **MROF-12**.

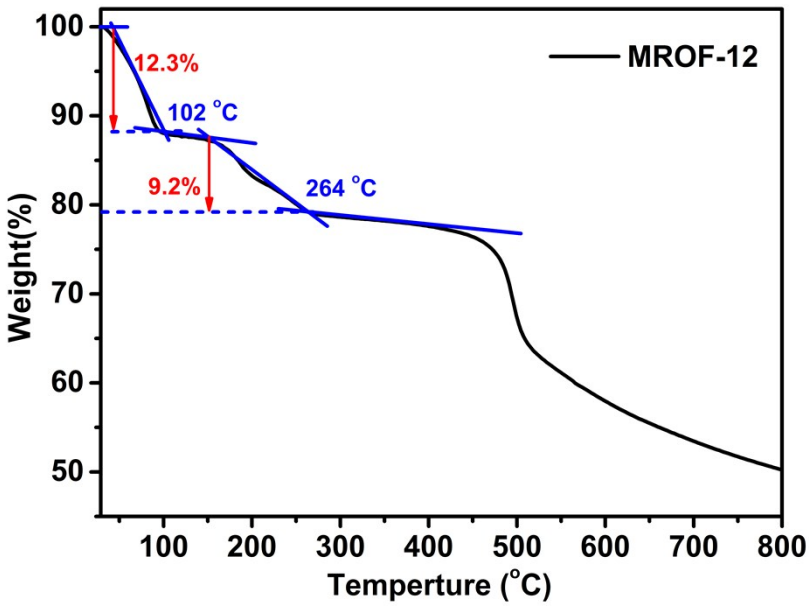

Figure S8. TGA curves for **MROF-12**.

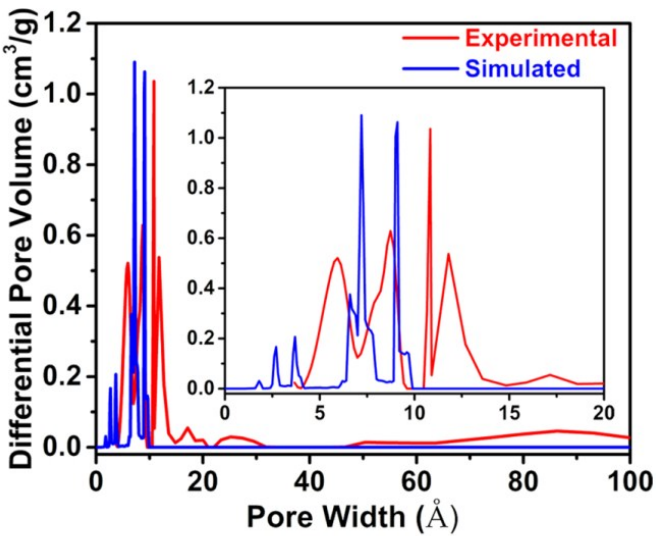

Figure S9. The pore-size distribution for Experimental and Simulated (simulated using the Zeo++ software package[6]).

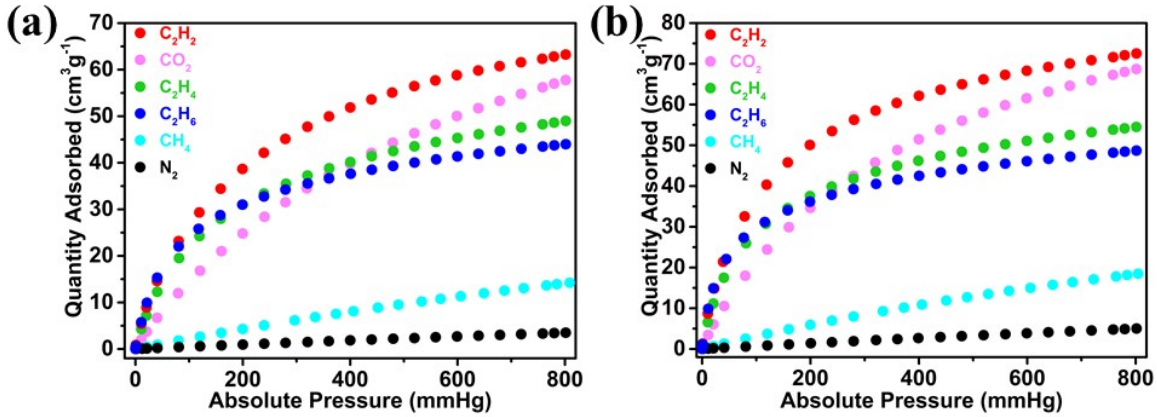

Figure S10. C_2H_2, CO_2, C_2H_4, C_2H_6, CH_4, N_2 sorption isotherms of **MROF-12a** at 296 K (a) and 273 K (b).

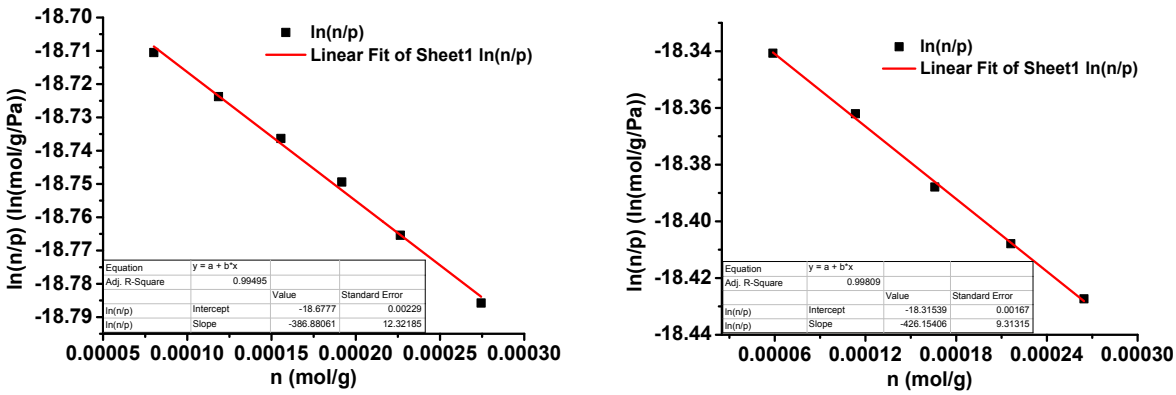

Figure S11. The virial graphs for adsorption of CH_4 on **MROF-12a** at 296 K (left) and 273 K (right).

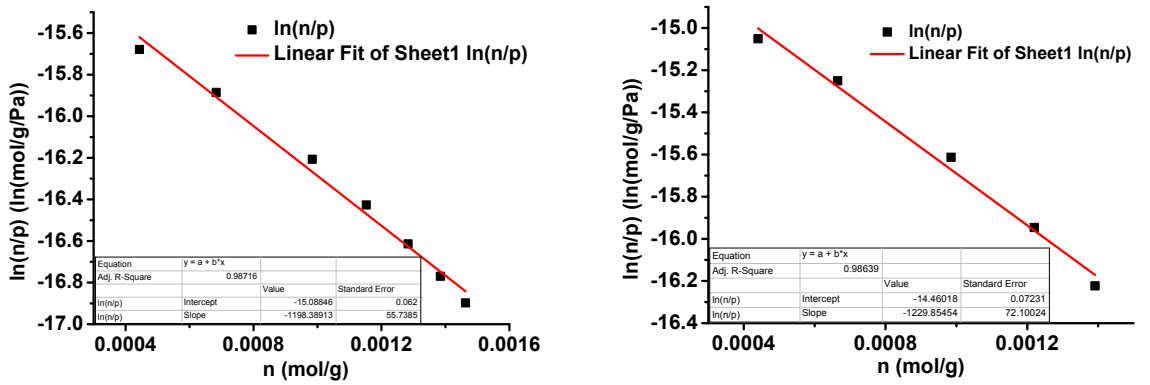

Figure S12. The virial graphs for adsorption of C_2H_6 on **MROF-12a** at 296 K (left) and 273 K (right).

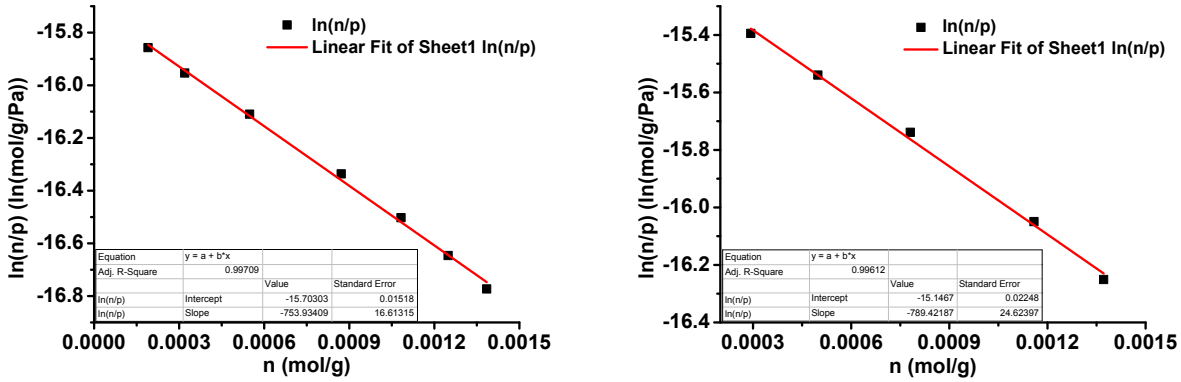

Figure S13. The virial graphs for adsorption of C_2H_4 on **MROF-12a** at 296 K (left) and 273 K (right).

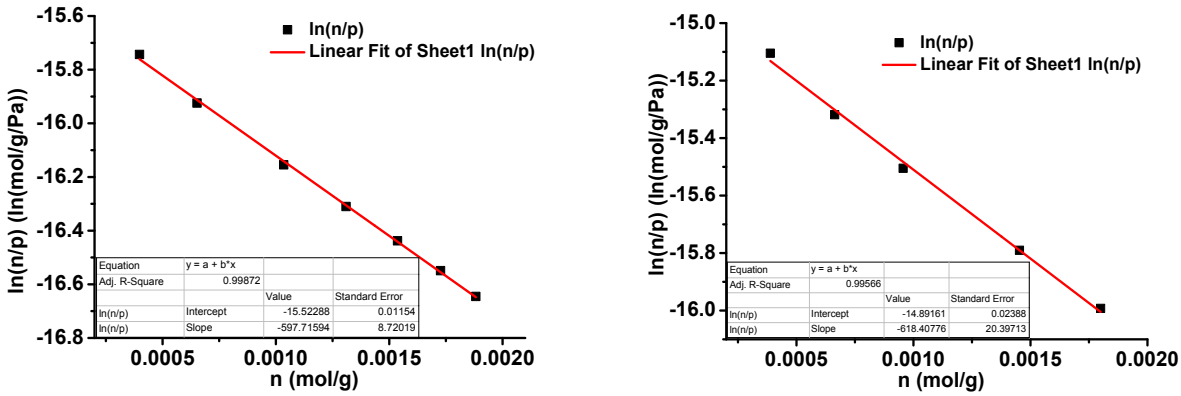

Figure S14. The virial graphs for adsorption of C_2H_2 on **MROF-12a** at 296 K (left) and 273 K (right).

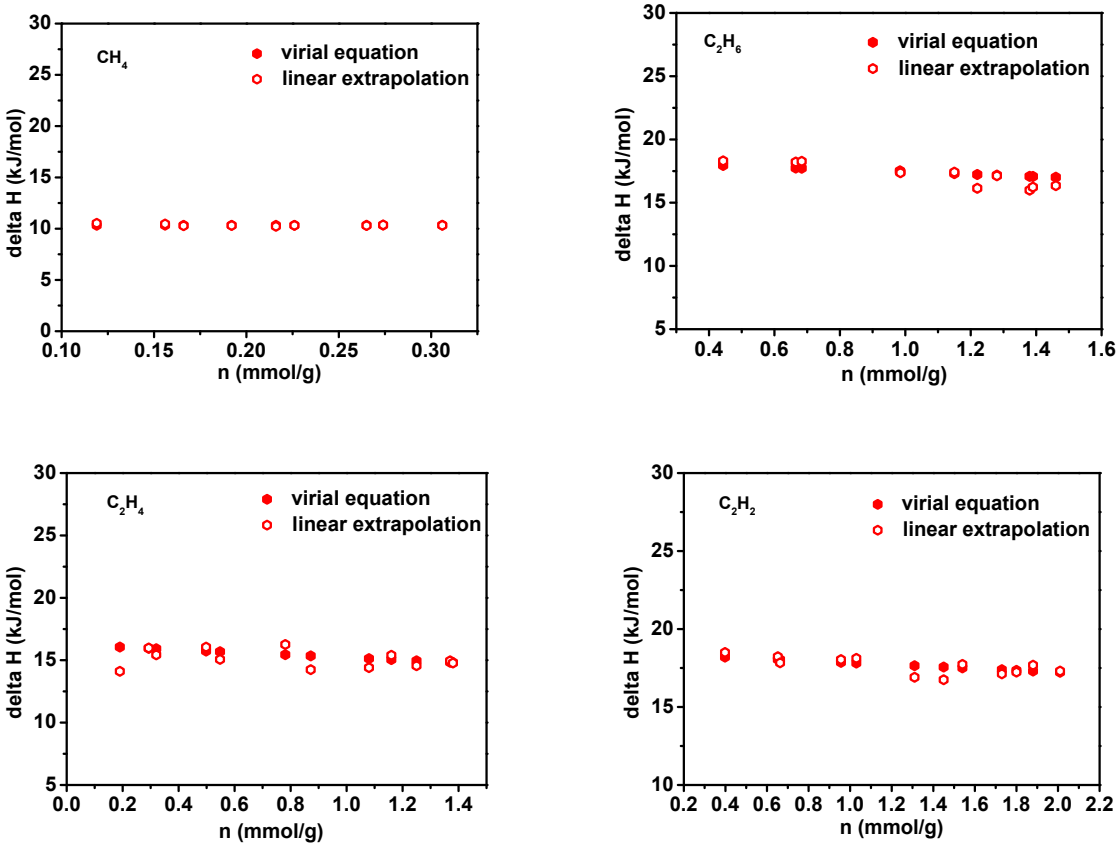

Figure S15. Comparison of the enthalpies for gas adsorption of CH_4, C_2H_6, C_2H_4, and C_2H_2 on **MROF-12a** from two methods: virial equation (solid) and linear extrapolation (open).

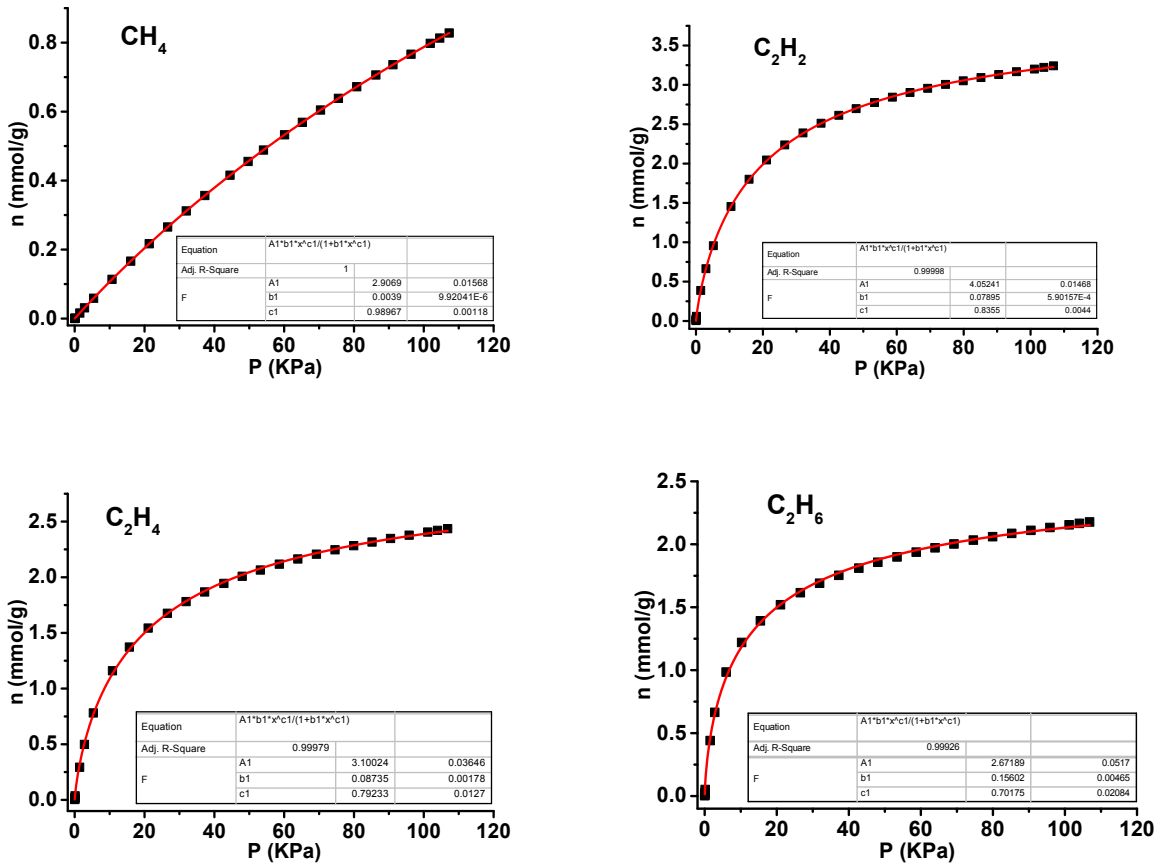

Figure S16. The graphs of the Single-site Langmuir-Freundlich equations fit for adsorption of CH_4, C_2H_2, C_2H_4 and C_2H_6 on **MROF-12a** at 273 K.

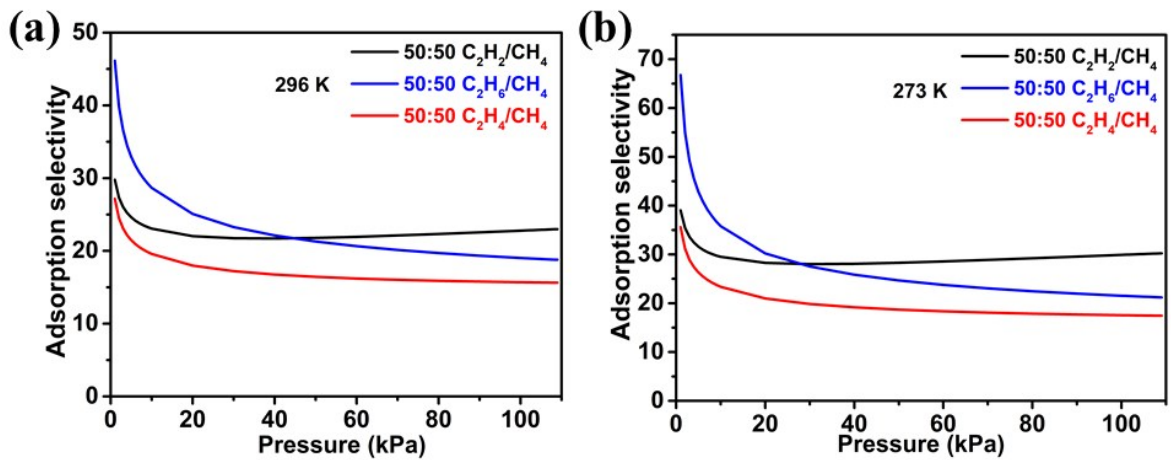

Figure S17. Comparison of the adsorption selectivity for equimolar C_2H_2/CH_4, C_2H_6/CH_4 and C_2H_4/CH_4 mixtures by IAST at 296 K (a) and 273 K (b) in **MROF-12a**.

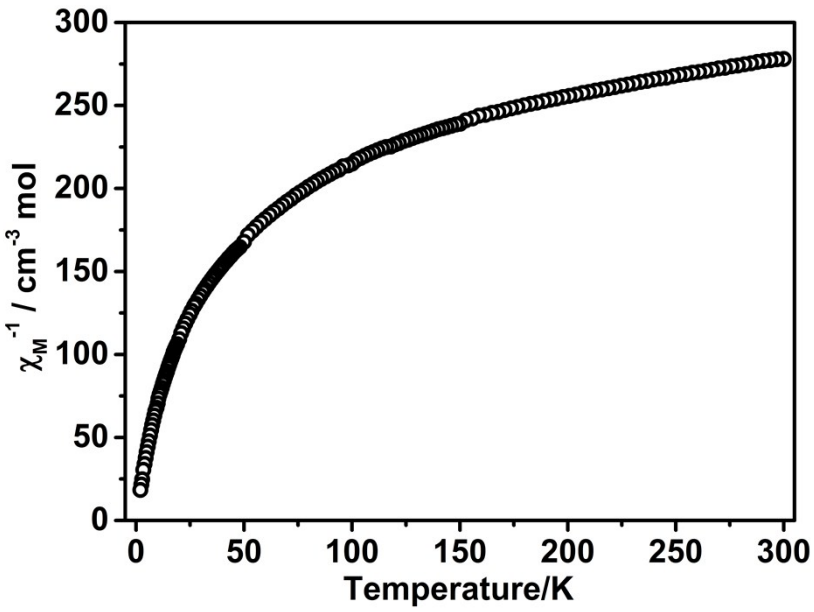

Figure S18. The χ_m^{-1} versus T plot of **MROF-12**.

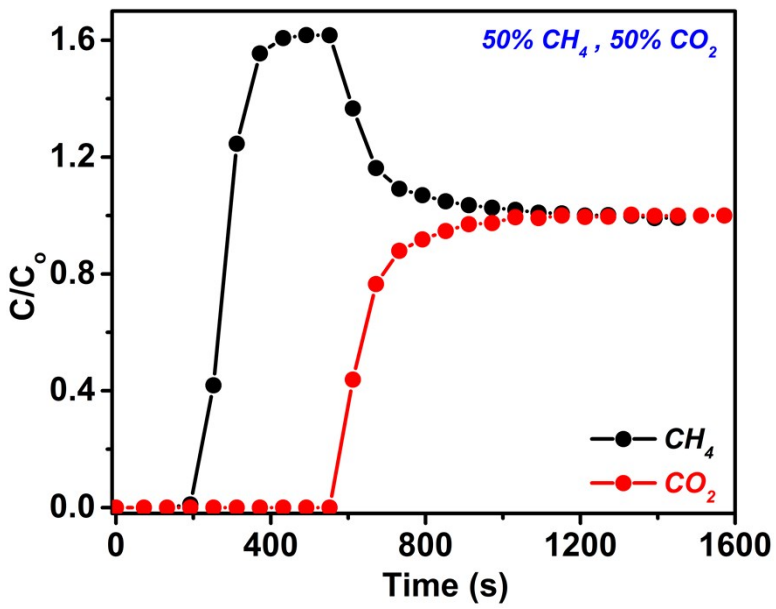

Figure S19. Column breakthrough experiment for a CO_2/CH_4 = 50/50 gas mixture was carried out on **MROF-12a** at 296 K and 1 bar.

The dynamic column breakthrough experiment is conducted by flowing the CO_2/CH_4 (50:50, v/v) mixture over a packed bed of the **MROF-12a** solid with a flow rate of 4.1 mL min^{-1}. From the breakthrough curve, it is can be known that the separation of the CO_2/CH_4 mixture can be efficiently achieved and CO_2 was not detected until a breakthrough time of 552 s. The dynamic CO_2 adsorption capacity for **MROF-12a** is 0.52 mmol g^{-1}, based on which, the separation factor was 1.50, and suggesting **MROF-12a** is promising for the separation of CO_2/CH_4 mixture.

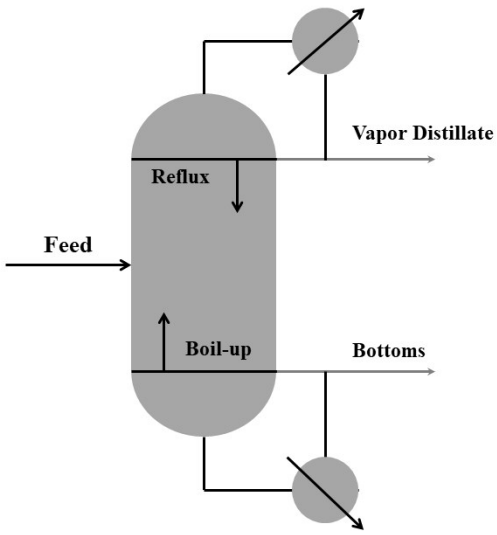

Figure S20. C_2H_2/CH_4 distillation system: Column configuration and specification for simulation by ASPEN PLUS.[7]

A distillation system was simulated using the process simulation platform, Aspen Plus, for the purpose of energy efficiency. A C_2H_2/CH_4 gas mixture in equimolar ratio was fed at room temperature and 1 atm with the feed ratio of 100 kg/h. To locate the steady states, the effective liquid holdup and boil-up ratio are chosen as the continuation parameters. It is of interest to note that there is a sudden increase in CH_4 purity (99.99%) in vapor distillate was withdrawn at a rate of 8.5 kg/h which assures by the constant liquid holdup from the reboiler temperature of -156 ^{o}C. Based on these experimental parameters, the energy consumption for CH_4 is 89792.8 kJ/h or 169.0 kJ/mol.

However, the C_2H_2 purity (99.9%) increased in bottoms and obtained at a rate of 5.828 kg/h when the reboiler temperature rises to -97 ^{o}C. At this point, the energy consumption for C_2H_2 is 24696.1 kJ/h or 110.2 kJ/mol.

Table S1. The diameter, stability, BET/Langmuir surface area and application for **MROF-12** and the reported MROFs.

Compounds	ligands	Cluster type	Diameter (Å)[a]	Heat Stability VXRD/TG (°C)	Chemical Stability (pH)	BET/Langmuir (m^2 g^{-1})	Application	Ref.
MROF-12	H_2NDI	$Cu_{12}(OH)_{12}(pz)_{12}$	12.202	400/481	2~13	460.7/571.9	Separation of C_2H_2/CH_4 and antiferromagnetism	This work
$Be_{12}(OH)_{12}(BTB)_4$	H_3BTB	$Be_{12}(OH)_{12}$	8.994	-/510	-	4030/4400	Hydrogen storage	8
MOF-520	H_3BTB	$Al_8(OH)_8(HCOO)_4$	8.670	-/502	-	2310/-	Coordinative alignment of molecules	9
CAU-1	NH_2-H_2BDC	$Al_8(OH)_4(OCH_3)_8$	8.114	310/360	-	-/1700	High porosity and thermal stability	10
MIL-125	H_2BDC	$Ti_8(O)_8(OH)_4$	8.247	360/350	-	1550/-	Reversible photochromic behavior	11
MROF-1	H_2thb, H_2pbdc	$In_6(thb)_6$	20.990	160/300	-	80.8/129.0	Proton conductivity	5
$H_2Na_4[Cu_{12}(OH)_6(pz)_6(BTC)_6]$	H_3BTC	$Cu_{12}(OH)_6(pz)_6$	12.185	250/220	-	813/-	Ion-exchange	4
CAU-3-BDC	H_2BDC	$Al_{12}(OCH_3)_{24}$	10.770	-/200	-	1250/1520	Sorption properties	12
CAU-3-BDC-NH_2	NH_2-H_2BDC	$Al_{12}(OCH_3)_{24}$	10.449	-/180	-	1550/1920		
CAU-3-NDC	H_2NDC	$Al_{12}(OCH_3)_{24}$	10.882	-/180	-	2320/2750		
MIL-125-NH_2	NH_2-BDC	$Ti_8(O)_8(OH)_4$	8.269	-	-	775/-	Photo-catalytic properties	13

On the whole, the difference not only present in the structures of the three MOFs (**MROF-12**, MROF-1 and $H_2Na_4[Cu_{12}(OH)_6(pz)_6(BTC)_6]\cdot 23H_2O$), but also in the performance for them. The stability of **MROF-12** is generally higher than that of the other two MOFs. In addition, unlike MROF-1 and $H_2Na_4[Cu_{12}(OH)_6(pz)_6(BTC)_6]\cdot 23H_2O$, multifunctional **MROF-12** adopts the unique functionalities of the metalloring clusters which endow its material with antiferromagnetism, and simultaneously inherits the porous properties of MOFs and can be used to the separation of C_2H_2/CH_4 mixture gases.

Table S2. Crystallographic Data and Structural Refinement Summary.

	MROF-12
CCDC	1835951
empirical formula	$C_{48}H_{36}Cu_4N_{12}O_{12}$
formula weight	1227.05
Temperature	100 K
Radiation	CuKα (λ = 1.54184 Å)
crystal system	trigonal
space group	*P*3
Dimensions	3D
a(Å)	26.0992(4)
b (Å)	26.0992(4)
c (Å)	9.2584(2)
α	90°
β	90°
γ	120°
Volume (Å^3)	5461.6(2)
Z	3
Density (calcd)	1.119 g/cm^3
Absorption	1. 755 mm^{-1}
Goodness-of-fit on F^2	1.047
F(000)	1860.0
*R*1, *wR*2 [$I>2\sigma(I)$][(a)]	0.0421, 0.0758
*R*1, *wR*2 (all data)[(a)]	0.0618, 0.0795

(a) $R_1 = \sum ||F_O| - |F_C|| / \sum |F_O|$; $wR_2 = \left[\sum w\left(|F_O|^2 - |F_C|^2\right)^2 / \sum w\left(F_O{}^2\right)^2\right]^{1/2}$

Table S3. Selected bond lengths [Å] for **MROF-12**.

Atom-Atom	bond lengths [Å]	Atom-Atom	bond lengths [Å]
Cu1-N1	1.954(6)	Cu3-N4	1.955(6)
Cu1-O1	1.950(7)	Cu3-N5	1.961(6)
Cu1-N9[1]	1.968(6)	Cu3-O2	1.974(6)
Cu1-O4[2]	1.947(7)	Cu3-O3	1.964(7)
Cu2-N3	1.961(6)	Cu4-N6	1.970(6)
Cu2-N2	1.967(6)	Cu4-N10[3]	1.979(6)
Cu2-O2	1.954(7)	Cu4-O4	1.962(7)
Cu2-O1	1.970(7)	Cu4-O3	1.961(7)

[1] -1+y-x, -1-x, 1+z;[2] -y, +x-y, +z; [3] -y, 1+x-y, 1+z.

Table S4. Selected bond angles [°] for **MROF-12**.

Atom-Atom-Atom	Angle/°	Atom-Atom-Atom	Angle/°	Atom-Atom-Atom	Angle/°
N1-Cu1-N9[1]	100.3(2)	N2-Cu2-O1	84.8(3)	N5-Cu3-O3	86.1(3)
O1-Cu1-N1	85.6(3)	O2-Cu2-N3	85.2(3)	O3-Cu3-O2	88.9(3)
O1-Cu1-N9[1]	171.4(3)	O2-Cu2-N2	171.9(3)	N6-Cu4-N10[3]	99.4(2)
O4[2]-Cu1-N1	170.8(3)	O2-Cu2-O1	91.0(3)	O4-Cu4-N6	171.5(3)
O4[2]-Cu1-O1	89.0(3)	N4-Cu3-N5	100.2(2)	O4-Cu4-N10[3]	85.1(3)
O4[2]-Cu1-N9[1]	85.9(3)	N4-Cu3-O2	85.7(3)	O3-Cu4-N6	85.4(3)
N3-Cu2-N2	99.9(2)	N4-Cu3-O3	171.0(3)	O3-Cu4-N10[3]	171.6(3)
N3-Cu2-O1	171.6(3)	N5-Cu3-O2	171.2(3)	O3-Cu4-O4	91.1(3)

[1] -1+y-x, -1-x, 1+z; [2] -y, +x-y, +z; [3] -y, 1+x-y, 1+z.

Table S5. The representative 3D MOFs that form by 12-connected cluster and linear linker.

Compounds	Nodes		Topology / Schläfli symbol	Ref.
MROF-12	$[Cu_{12}(\mu_2\text{-}OH)_{12}(Pz)_{12}]$	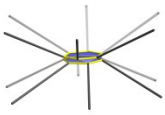	$-/4^{60}\cdot6^{6}$	This work
MROF-1	$[In_6(thb)_6(CO_2)_{12}]^{6-}$	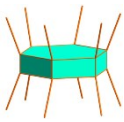	$-/4^{60}\cdot6^{6}$	9
Ce-UiO-66-BPyDC	$[Ce_6(\mu_3\text{-}O)_4(\mu_3\text{-}OH)_4(CO_2)_{12}]$	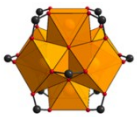	*fcu*/-	14
RE-fcu-MOF (RE = Y, Tb)	$[RE_6(\mu_3\text{-}OH)_8(CO_2)_{12}]$		*fcu*/-	15
UiO-66	$[Zr_6O_4(OH)_4(CO_2)_{12}]$	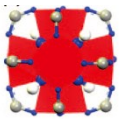	*fcu*/-	16
CAU-1	$\{Al_8(OH)_4(OCH_3)_8\}^{12+}$	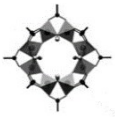	-/-	6
CAU-3	$[Al_2(OCH_3)_4(CO_2)_2]$	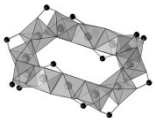	*fcu*/-	10
$[Zn_5(\mu_3\text{-}OH)_2(bdc)_2(bimf)_2]\cdot4H_2O$	$[Zn_5(\mu_3\text{-}OH)_2(CO_2)_7(C_3N_2)_4]$		*fcu*/-	17
RE-BDC/NDC (RE = Y, Tb, Er)	$[RE_3(\mu_3\text{-}OH)(COO)_6]$	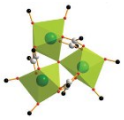	*hcp*/$3^{24}\cdot43^{3}\cdot5^{9}$	18
$[Cu_{12}Br_2(CN)_{6/2}(SCH_3)_6][Cu(SCH_3)_2]$	$[Cu_{12}(SCH_3)_6]^{6+}$		*pseudo-pcu*/-	19
$[Co_{12}(L)_6(\mu_3\text{-}PO_4)_4(\mu_3\text{-}F)_4(\mu\text{-}H_2O)_6][NO_3]_2$	$[Co_{12}(\mu\text{-}RCO_2)_{12}(\mu_3\text{-}PO_4)_4(\mu_3\text{-}F)_4(\mu\text{-}H_2O)_6]^{4-}$		*fcu*/-	20

Table S6. Virial graph analyses data for **MROF-12a** and its C_2/C_1 separation selectivities ($C_2 = C_2H_2$, C_2H_4, C_2H_6; $C_1 = CH_4$).

Material	adsorbate	*T*/K	A_0/ ln(mol g^{-1} Pa^{-1})	A_1/ g mol^{-1}	R^2	K_H/ mol g^{-1} Pa^{-1}	S_i/ $_{CH4}$[a]	ΔH/kJ mol^{-1}
MROF-12a	C_2H_2	296	-15.522	-597.716	0.998	1.815×10^{-7}	23.4	17.8
		273	-14.892	-618.408	0.996	3.408×10^{-7}	30.7	
	C_2H_4	296	-15.703	-753.934	0.997	1.515×10^{-7}	19.6	15.4
		273	-15.147	-789.422	0.996	2.641×10^{-7}	23.8	
	C_2H_6	296	-15.088	-1198.389	0.987	2.801×10^{-7}	36.2	17.4
		273	-14.460	-1229.855	0.986	5.249×10^{-7}	47.2	
	CH_4	296	-18.678	-386.881	0.994	7.731×10^{-9}	1.0	10.3
		273	-18.315	-426.154	0.996	1.111×10^{-8}	1.0	

[a]The Henry's law selectivity for gas component *i* over CH_4 at the speculated temperature is calculated based on the equation $S_{ij} = K_{H(i)}/K_{H(j)}$.

Table S7. Comparison of several representative porous materials for the practical separation of C_2H_2/CH_4.

Materials	Gas mixtures	Temperature (K)	Total flow (mL min^{-1})	Separation factor	C_2H_2 adsorption capacity (mmol/g)	Q_{st} (kJ/mol)		Ref.
						C_2H_2	CH_4	
MROF-12a	$C_2H_2/CH_4/He$ (5/5/90)	298	6.5	6.82	0.29	17.8	10.3	This work
s-PMO-2	$C_2H_2/CH_4/He$ (5/5/90)	298	4	5.2	0.13	25.0	12.3	21
ZJNU-59	C_2H_2/CH_4 (50/50)	298	5	26.2	4.2	31.8	-	22
ZJNU-54	C_2H_2/CH_4 (50/50)	298	5	39.5	6.57	35.4	16.8	23
SNNU-95	C_2H_2/CH_4 (50/50)	273	6	-	2.69	47.2	-	24
NKMOF-1-Ni	C_2H_2/CH_4 (50/50)	298	1.6	6.6	-	60.3	31.7	25
Industrial technologies	C_2H_2/CH_4 (50/50)	296	-	-	-	110.2	169.0	Figure S20

References

1 I. P. O'koye, M. Benham and K. M. Thomas, *Langmuir,* 1997, **13**, 4054–4059.
2 A. L. Myers and J. M. Prausnitz, *AIChE J.,* 1965, **11**, 121.
3 (a) Z. Y. Li, Z. J. Zhang, Y. X. Ye, K. C. Cai, F. F. Du, H. Zeng, J. Tao, Q. J. Lin, Y. Zheng and S. C. Xiang, *J. Mater. Chem. A,* 2017, **5**, 7816–7824; (b) J. G. Li, J. Gao, H. Li, X. F. Yang and Y. Liu, *Anal. Methods,* 2014, **6**, 4305–4311.
4 Y. H. Han, Y. X. Ye, C. Tian, Z. J. Zhang, S. W. Du and S. C. Xiang, *J. Mater. Chem. A,* 2016, **4**, 18742–18746.
5 H. Zhang, Y. Lu, Z. Zhang, H. Fu, Y. Li, D. Volkmer, D. Denysenko and E. Wang, *Chem. Commun.,* 2012, **48**, 7295–7297.
6 T. F. Willems, C. H. Rycroft, M. Kazi, J. C. Meza and M. Haranczyk, *Microporous Mesoporous Mater.*, 2012, **149**, 134–141.
7 (a) G. Z. Zuo, R. Wang, R. Field and A. G. Fane, *Desalination*, 2011, 283, 237–244; (b) B. Yang, J. Wu, G. S. Zhao, H. J. Wang and S. Q. Lu, *Chinese J. Chem. Eng.*, 2006, 14, 301–308.
8 K. Sumida, M. R. Hill, S. Horike, A. Dailly and J. R. Long, *J. Am. Chem. Soc.,* 2009, **131**, 15120–15121.
9 S. Lee, E. A. Kapustin and O. M. Yaghi, *Science,* **2016**, *353*, 808–811.
10 T. Ahnfeldt, N. Guillou, D. Gunzelmann, I. Margiolaki, T. Loiseau, G. Férey, J. Senker and N. Stock, *Angew. Chem.,* 2009, **121**, 5265–5268.
11 M. Dan-Hardi, C. Serre, T. Frot, L. Rozes, G. Maurin, C. Sanchez and G. Férey *J. Am. Chem. Soc.,* 2009, **131**, 10857–10859.
12 H. Reinsch, M. Feyand, T. Ahnfeldt and N. Stock, *Dalton Trans.,* 2012, **41**, 4164–4171.
13 A. P. Smalley, D. G. Reid, J. C. Tan and G. O. Lloy, *CrystEngComm,* 2013, **15**, 9368–9371.
14 M. Lammert, C. Glißmann, H. Reinsch and N. Stock, *Cryst. Growth Des.,* 2017, **17**, 1125−1131.
15 A. H. Assen, Y. Belmabkhout, K. Adil, P. M. Bhatt, D.-X. Xue, H. Jiang and M. Eddaoudi, *Angew. Chem. Int. Ed.,* 2015, **54**, 14353–14358.
16 J. H. Cavka, S. Jakobsen, U. Olsbye, N. Guillou, C. Lamberti, S. Bordiga and K. P. Lillerud, *J. Am. Chem. Soc.,* 2008, **130**, 13850–13851.
17 H. Guo, X. Guo, H. Zou, Y. Qi and R. Chen, *CrystEngComm,* 2014, **16**, 2176–2187.
18 N. Wei, R.-X. Zuo, Y.-Y. Zhang, Z.-B. Han and X.-J. Gu, *Chem. Commun.,* 2017, **53**, 3224–3227.
19 X. Liu and K.-L. Huang, *Inorg. Chem.* 2009, **48**, 8653–8655.
20 S. A. K. Robinson, M.-V. L. Mempin, A. J. Cairns and K. T. Holman, *J. Am. Chem. Soc.,* 2011, **133**, 1634–1637.
21 L. Wu, Z. Yu, Y. X. Ye, Y. Yang, H. Zeng, J. Huang, Y. Huang, Z. J. Zhang and S. C. Xiang, *J. Solid State Chem.*, 2018, **264**, 113–118.
22 Y. Wang, M. He, X. Gao, S. Li, S. Xiong, R. Krishna and Y. B. He, *ACS Appl. Mater. Interfaces*, 2018, **10**, 20559−2056.
23 J. Jiao, L. Dou, H. Liu, F. Chen, D. Bai, Y. Feng, S. S. Xiong, D. L. Chen and Y. He, *Dalton Trans.*, 2016, **45**, 13373–13382.
24 H. Li, S. Li, X. Y. Hou, Y. C. Jiang, M. Hu and Q.-G. Zhai, *Dalton Trans.*, 2018, **47**, 9310–9316.
25 Y.-L. Peng, T. Pham, P. Li, T. Wang, Y. Chen, K.-J. Chen, K. A. Forrest, B. Space, P. Cheng, M. J. Zaworotko and Z. J. Zhang, *Angew. Chem., Int. Ed.*, 2018, **57**, 10971–10975.